Numerical simulation of the fluid structure interactions in a compliant patient-specific arteriovenous fistula

Iolanda Decorato [1], Zaher Kharboutly [1], Tommaso Vassallo [1], Justin Penrose [2], Cécile Legallais [1] and Anne-Virginie Salsac [1,*,†]

[1]*Biomechanics and Bioengineering Laboratory (UMR CNRS 7338), Université de Technologie de Compiègne, 60203 Compiègne, France*
[2]*ANSYS UK Limited, 97 Milton Park, OX14 4RY, United Kingdom*

SUMMARY

The objective of the study is to investigate numerically the fluid-structure interactions (FSI) in a patient-specific arteriovenous fistula (AVF) and analyze the degree of complexity that such a numerical simulation requires to provide clinically relevant information. The reference FSI simulation takes into account the non-Newtonian behavior of blood, as well as the variation in mechanical properties of the vascular walls along the AVF. We have explored whether less comprehensive versions of the simulation could still provide relevant results. The non-Newtonian blood model is necessary to predict the hemodynamics in the AVF because of the predominance of low shear rates in the vein. An uncoupled fluid simulation provides informative qualitative maps of the hemodynamic conditions in the AVF; quantitatively, the hemodynamic parameters are accurate within 20% maximum. Conversely, an uncoupled structural simulation with non-uniform wall properties along the vasculature provides the accurate distribution of internal wall stresses, but only at one instant of time within the cardiac cycle. The FSI simulation advantageously provides the time-evolution of both the hemodynamic and structural stresses. However, the higher computational cost renders a clinical use still difficult in routine. Copyright © 2013 John Wiley & Sons, Ltd.

1. INTRODUCTION

Hemodialysis is conducted in patients with end-stage renal disease in order to filter blood waste products and compensate for the ill-functioning kidneys. To enable hemodialysis, a partial extracorporeal circulation needs to be set up toward the artificial kidney. It requires a permanent vascular access that is easily available for a repeated use and that provides a blood flow larger than 500 ml·min^{-1} [1, 2]. The most standard technique is to create in the arm an arteriovenous fistula (AVF) by connecting a vein onto an artery (e.g., the cephalic vein onto the radial artery in the case of an end-to-side AVF) [3]. Subjected to arterial pressure, the vein gets arterialized after 3 to 6 months [4]. Once mature, the fistula behaves as a low resistance, high compliance pathway between the high pressure arterial system and the low pressure venous system [3].

The lifespan of an AVF is limited from a few days to about 10 years because of the onset of complications [3]. Some complications may affect directly the AVF, such as atherosclerotic plaques, stenoses, or aneurysms [3, 5]. In practice, the AVF failure is caused by an insufficient or excessive blood flow inside the vein, compromising either the hemodialysis procedure [6] or the cardiac load.

---

*Correspondence to: Anne-Virginie Salsac, Université de Technologie de Compiègne, CS 60319, 60203 Compiègne, France.
†E-mail: anne-virginie.salsac@utc.fr

Hemodynamics plays an important role in the evolution and long-term efficiency of the AVF [6]. Non-invasive *in vivo* hemodynamic measurement techniques, such as echo-Doppler, can provide averaged velocity values [7] but neither velocity profiles nor wall shear stresses (WSS). The hemodynamics inside patient-specific fistula has previously been investigated through CFD simulations [8–10]. These studies have provided a comprehensive knowledge of the spatial and temporal distribution of the hemodynamics inside the AVF and shown direct correlations between altered WSS patterns and local vessel damages. They, however, assume the vascular wall to be rigid, which is not the case physiologically. No study has yet investigated the influence of the wall compliance on the hemodynamics in an AVF.

Over the last years, quite a few numerical models simulating the fluid-structure interactions (FSI) in the cardiovascular system have otherwise been developed ([11–17] among others). They are performed with a three-fold objective: to investigate how hemodynamic factors influence the onset and progression of cardiovascular diseases, to predict the outcome of surgical interventions, and to evaluate the effect and efficacy of medical devices [11, 18–22].

Our present objective is to study the influence of the wall compliance on the hemodynamics and wall mechanics in a patient-specific radio-cephalic AVF. Our goal is to perform the FSI simulation with one of the numerical software that clinicians could use to evaluate the hemodynamic and structural conditions within the AVF during the patients' follow up. For this purpose, we have chosen to simulate the FSI with the commercial code ANSYS Workbench (ANSYS, Inc.). We have modeled the hyperelastic behavior of the vessel walls as well as the difference in wall thickness and mechanical properties of the cephalic vein and radial artery.

In a second part of the study, we have analyzed whether it is possible to reduce the computational time of the simulation in the perspective of translating the numerical tool to clinicians. We have relaxed independently the different assumptions concerning the material properties and the strong coupling of the fluid and solid physics and compared the results with those obtained with the more comprehensive model.

2. MATERIAL AND METHODS

2.1. *Patient-specific arteriovenous fistula geometry and meshing*

The case of study is a mature end-to-side radio-cephalic fistula. The medical images of the complete AVF lumen have been acquired by CT-scan angiography at the Polyclinique Saint Côme (Compiègne, France). During the clinical measurements, the patient was at rest in supine position.

The images have been segmented and the complete AVF lumen has been reconstructed following the method described by Kharboutly *et al.* [23]. In order to image the artery and the vein during the same acquisition, a contrast bolus was injected in the patient's opposite arm. The amount of contrast agent was dosed to optimize the image contrast and resolution in both vessels. The best volume reconstruction was obtained by applying a combination of intensity and gradient forces and a smoothness constraint based on the curvature of the surface. The reconstructed vascular geometry is shown in Figure 1.

The AVF presents an 80%-stenosis along the proximal radial artery and an enlargement in the cephalic vein. The artery is 170 mm long and has an internal diameter of 5.95 mm at the inlet and 6.25 mm at the outlet. The outlet venous diameter is 10 mm. The inlet cross-section is denoted S_a^i and the outlet ones S_a^o on the arterial side and S_v^o on the venous side. Throughout the paper, the subscript v stands for vein and a for artery.

The fluid mesh is generated using the software T-GRID (ANSYS, Inc.). We first mesh the lateral surface of the lumen and then generate the volume mesh of the fluid domain. The latter consists of a hybrid mesh, with seven prismatic cells in the boundary layer and tetrahedral cells in the vessel core (see [23] for more details on the mesh generation).

The structural part of the vessel wall is then modeled as a monolayer of discrete-Kirchhoff theory-based shell finite elements. They are four-node linear triangular shell elements. Different thicknesses have been imposed to the arterial and venous shell elements. Thickness data have been taken from the literature, as no direct measurement was possible *in vivo*. We have modeled the vein with a
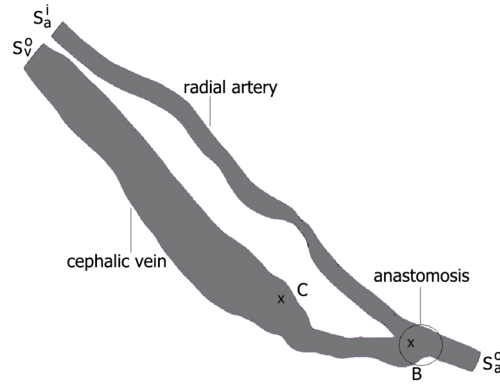
Figure 1. Schematics of the vascular geometry. S_a^i represents the arterial inlet, S_a^o is the arterial outlet, and S_v^o is the venous outlet. Points B and C are the two locations with the highest temporal gradients of wall shear stresses.

thickness of 0.4 mm, which is typical for a cephalic vein prior to the AVF creation. Indeed, the vein thickness tends to remain altogether constant during fistula maturation [24]. The arterial thickness is supposed to be equal to $1/10^{th}$ of the actual inlet diameter, which is 0.6 mm [25]. The fluid and solid meshes share the same nodes at the interface.

We have investigated the convergence of the numerical results with the mesh spatial resolution. The convergence study, reported in Decorato *et al.*[‡], has shown that a maximum mesh size of 4×10^{-3} mm guarantees errors below 0.8% both for the maximum velocity magnitude and WSS. This characteristic mesh size appears as a good compromise between numerical accuracy and computational time. The whole mesh is hence composed of 784×10^3 fluid elements and 89×10^3 shell elements for the walls.

2.2. Blood model

Blood is modeled as an isotropic, homogeneous, non-Newtonian fluid. It is assumed to follow Casson model

$$\sqrt{\tau} = \sqrt{\tau_0} + \sqrt{\kappa \dot{\gamma}},$$ (1)

where τ_0 represents the yield stress, $\dot{\gamma}$ is the shear rate, and κ is the consistency. The Casson model has been largely used in the literature to model blood rheology [26]. It has been found to provide a more precise WSS distribution at the vessel walls as compared to the Carreau-Yasuda model [27]. The apparent viscosity μ is obtained from Equation (1) and reads

$$\sqrt{\mu} = \sqrt{\frac{\tau_0}{\dot{\gamma}}} + \sqrt{\kappa}.$$ (2)

The model parameters have been chosen according to experimental data obtained at low shear rates: $\tau_0 = 4 \times 10^{-3}$ Pa, $\kappa = 3.2 \times 10^{-3}$ Pa·s [28]. In Section 4.1, we will compare the results obtained using Casson blood model with those predicted modeling blood as a Newtonian fluid. Blood density is set to 1050 kg·m^{-3}.

[‡]Decorato I, Salsac A-V, Legallais C, Ali-Mohammadi M, Diaz-Zuccarini V, Kharbouthly Z. Impact of the degree of residual stenosis after balloon-angioplasty in arteriovenous fistulae. *Medical & Biological Engineering & Computing* 2013

2.3. *Vessel wall properties*

We simulate the vessel wall hyperelasticity assuming both the artery and the vein to follow the 3rd-order Yeoh model [29]. The strain energy function ψ reads

$$\psi = C_{10}(I_1 - 3) + C_{20}(I_1 - 3)^2 + C_{30}(I_1 - 3)^3 + \\ D_1(J - 1)^2 + D_2(J - 1)^4 + D_3(J - 1)^6,$$

(3)

where I_1 is the deviatoric first principal strain invariant and J is the Jacobian. The parameters are the material constants C_{10}, C_{20}, and C_{30} and the incompressibility parameters D_1, D_2, and D_3. The vessel wall is assumed to be incompressible (i.e., $J = 1$). We have differentiated the arterial and venous mechanical properties in order to correctly model the larger compliance of the artery as compared to the arterialized vein. The experimental data ([30] for the vein and [31] for the artery) are fitted with the Yeoh model as shown in Figure 2. The coefficient of determination is equal to $R^2 = 0.985$ for the artery and 0.985 for the vein. The model constants are provided in Table I.

2.4. *Boundary conditions*

All the boundary conditions imposed for the fluid and solid domains are summarized in Table II. For the fluid flow, we impose a time-dependent flat velocity profile V_a^i at the inlet and time-dependent
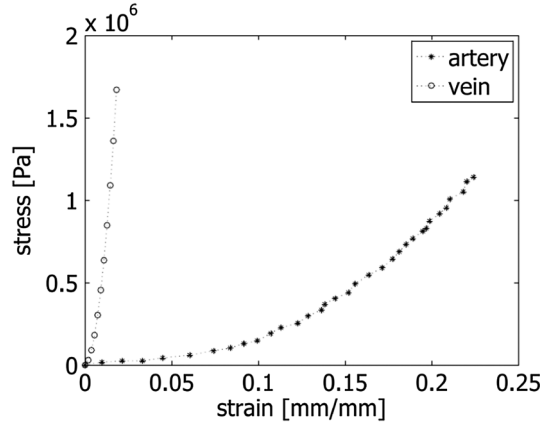

Figure 2. Mechanical behavior imposed to the radial artery and cephalic vein. The experimental data have been taken from McGilvray *et al*. [30] for the vein and Prendergast *et al*.[31] for the artery and fitted with a 3rd order Yeoh model.

Table I. Values of the constants of the hyperelastic 3rd-order Yeoh model used for the radial artery and the cephalic vein.

Constant	Artery	Vein
C_{10}	0.763×10^5 Pa	3.784×10^6 Pa
C_{20}	3.697×10^5 Pa	5.543×10^8 Pa
C_{30}	5.301×10^5 Pa	6.491×10^9 Pa

Table II. Boundary conditions imposed at the extremities of the fluid and solid domains (see Figure 1 for the surface definitions).

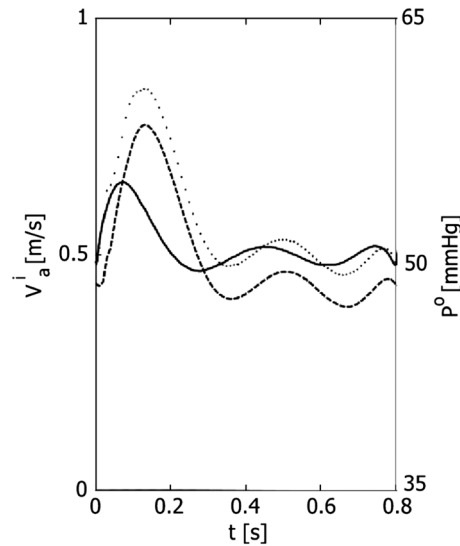| Boundary	Fluid domain	Solid Domain
S_a^i	Time-dependent velocity profile V_a^i	0-translation, 0-rotation
S_a^o	Time-dependent pressure profile P_a^o	0-translation, 0-rotation
S_v^o	Time-dependent pressure profile P_v^o	0-translation, 0-rotation
Vessel wall	No-slip condition	Atmospheric pressure

Figure 3. Waveforms of the inlet velocity profile V_a^i (continuous line) and outlet pressures P_a^o (dotted line) for the radial artery and P_v^o (marked line) for the cephalic vein.

pressure profiles at the arterial and venous outlets (Figure 3). The velocity, prescribed at the inlet of the proximal radial artery (S_a^i in Figure 1), is the one that was measured by echo-Doppler on the patient on the same day as the CT-scan angiography [9]. The imposed velocity corresponds to a systolic Reynolds number of 1230, time-averaged Reynolds number of 1020, and Womersley number of 4. A space-varying velocity profile following the Womersley solution [32] is recovered in the radial artery 8 diameters downstream of the inlet boundary. A fully developed profile therefore enters the stenosis, located about 16 diameters from the entrance.

The *in vivo* measurements do not provide any pressure data, as pressure measurements are invasive, but only the value of the flow split between the arterial (S_a^o) and venous (S_v^o) outlets (30%-70%, respectively). In order to deduce the pressure waveforms at the outlets, we have conducted a CFD simulation using ANSYS-CFX (ANSYS, Inc.). As inlet velocity, we set V_a^i. At the two outlets, we impose an R-C Windkessel model, following the method described in Decorato *et al.*[‡] The values of the parameters of the Windkessel model have been calculated so that

- the flow split between the arterial and venous outlets is 30%–70%;
- the time-averaged inlet pressure $\overline{P}_a^i$ is about 70 mmHg [6].

Neither rotation nor translation is allowed at the vascular extremities of the solid domain. The external tissues are supposed to be at atmospheric pressure, which is the pressure of reference in the FSI simulation.

2.5. Numerical method

The transient FSI are simulated inside the AVF using ANSYS Workbench V13.0 (ANSYS, Inc.). It implicitly couples a fluid solver (ANSYS CFX) to solve the blood flow with a solid solver (ANSYS-Mechanical) to solve the vascular wall deformation [33]. The software is based on an arbitrary Lagrangian–Eulerian formulation. The fluid solver resolves the fluid continuity and momentum equations in their conservative convection-diffusion form [33]. These equations are solved implicitly with the Rhie–Chow interpolation method [34]. The structural solver, based on an FEM, uses a Lagrangian multiplier-based mixed u-P formulation and assumes large displacements.

[‡]Decorato I, Salsac A-V, Legallais C, Ali-Mohammadi M, Diaz-Zuccarini V, Kharbouthly Z. Impact of the degree of residual stenosis after balloon-angioplasty in arteriovenous fistulae. *Medical & Biological Engineering & Computing* 2013

The FSI problem is solved using a partitioned approach with stagger iterations within each time step. During each stagger iteration:

– The displacement vectors are transferred from the structural to the fluid solver, where the fluid problem is solved for the current time-step;
– The load vectors are then transferred from the fluid to the structural solver, where the structural problem is solved;
– The convergence of all field equations (fluid and structural) is evaluated.

Stagger iterations are repeated until all the field equations have converged and the coupling conditions are satisfied at the fluid–solid interface. The latter requires that (i) displacements of the fluid and solid domains are compatible, (ii) forces acting on the interface are at equilibrium, and (iii) the fluid obeys the no-slip condition. The criterion for convergence has been set at 10^{-4} for all the fields. Apart from the first time step, which may require up to 50 sub-iterations for convergence to be achieved, convergence is otherwise reached within less than 15 iterations through the entire simulation.

The simulations are run neglecting gravity. The reference pressure is the atmospheric pressure. As initial condition, we use the results obtained from a steady fluid-only simulation, in which we impose the time-averaged values of the velocity and pressures as boundary conditions.

We have searched for the optimal time-step for which (i) the numerical model is stable, (ii) the computational time is the smallest, and (iii) the temporal resolution is sufficient to capture the time-dependent flow features. We have tested three time steps: 10^{-3}, 5×10^{-3}, and 10^{-2} s. We find that the simulation is unstable with the time of 10^{-2} s but remains stable with the two smaller values. The numerical scheme is therefore conditionally stable, with a limit of stability between 5×10^{-3} and 10^{-2} s. Reducing the time step by a factor of 5 hardly has an effect on the accuracy of the results: the WSS calculated with a time step of 5×10^{-3} s differ by less than 1% from those obtained with 10^{-3} s. It, however, has a direct impact on the computational time, which increases linearly with the number of iterations. We have therefore chosen to run all the following simulations with the time step of 5×10^{-3} s in order to optimize the computational time without loss in accuracy.

Each FSI simulation is run over six consecutive cardiac cycles. The repeatability of the results is verified after three cardiac cycles with cycle-to-cycle differences inferior to 1%. The results shown in the following are obtained by phase-averaging the field values over the 4th, 5th, and 6th cardiac cycles. The total simulation time is approximately 70 CPU hours on an Intel(R) Xeon(R) workstation with 64 bit CPU dual core processors of 2.67 GHz clock speed, 23.9 GB RAM memory and a Microsoft Windows XP operating system. The computation of the solution has been partitioned on the two cores using the default algorithm provided in ANSYS 13.0 (ANSYS, Inc.).

Instability issues due to the similar densities of the fluid and solid parts have been solved reducing the under-relaxation factor below the default value of 0.7. However, under-relaxation factors below 0.05 have been observed to induce non-physiological effects in our model. We have therefore chosen an under-relaxation factor equal to 0.08. It needs to be noticed that the optimal value of the under-relaxation factor may vary if the anatomical model changes.

2.6. *Wall shear stresses*

The WSS are contained within the plane tangent to the vascular wall, defined by the unit vector normal to the vessel wall **n**. They can be expressed by the two-component vector

$$\tau_w = \mu \frac{\partial \mathbf{v}}{\partial \mathbf{n}}, \tag{4}$$

where **v** is the velocity vector. We call WSS as the modulus of τ_w. In healthy arteries, physiological values of WSS are typically 1–2 Pa [6]. The physiological range is rather 0.8–3 Pa in healthy veins [35].

The oscillatory shear index (OSI)

$$OSI = 0.5 \left(1 - \frac{|\int_0^T WSS dt|}{\int_0^T |WSS| dt} \right), \tag{5}$$

where T is the time period of the cardiac cycle. The OSI index represents the degree of oscillation in the WSS orientation. Its values fall in the range $[0, 0.5]$, 0 corresponding to a constant forward flow and 0.5 to a purely oscillating flow. OSI values are typically below 0.2 in healthy physiological vessels. A value of 0.3–0.35 is considered as the threshold, above which neo-intimal activation might occur [36].

The time derivatives of WSS ($WSSG_t$) are defined as

$$WSSG_t = \frac{\partial WSS}{\partial t}. \tag{6}$$

They are typically small in healthy vessels. We will analyze which AVF zones are exposed to non-vanishing values of WSS time derivatives.

2.7. Internal wall stresses

To study the stresses within the vessel wall, we consider the Cauchy stress tensor σ. The stress tensor can be reduced to its principal components σ_i ($i = 1, 2, 3$) in the principal coordinate system. We study the distribution of the maximum component of the principal stresses

$$\sigma_{max} = max_i(\sigma_i), \tag{7}$$

and consider its time-averaged value $\overline{\sigma}_{max}$.

2.8. Validation of the flow simulations

The flow simulations have been validated by comparison with measurements obtained in a rigid mold of the patient-specific AVF geometry. A transparent phantom has been printed directly by rapid prototyping in poly(methyl methacrylate) (PFT Innovaltech, Saint Quentin, France) from the 3D volume reconstruction of the patient vasculature (Figure 4(a)). The printing technique consists of depositing poly(methyl methacrylate) microcapsules, which are subsequently liquified by means of a laser. The phantom walls are printed with a constant thickness. Connectors have been inserted between the arterial and venous branches of the AVF mold to ensure its solidity. All the experiments are conducted placing the phantom in a rectangular liquid-filled transparent box to optimize the mold transparency and match the indices of refraction.

Because the pulsatility of the inlet flow in the radial arterial is low (Figure 3), a constant flow rate of 1 l.min^{-1} has been imposed at the arterial inlet for the validation. It corresponds to the average arterial inlet flow rate measured on the patient. It is supplied by a peristaltic pump (Masterflex Easy-Load 7518-10, Cole-Parmer, Vernon Hills, IL, USA). In order to reproduce blood viscosity, the perfusing fluid is composed of 70% of water and 30% of glycerine (VWR, Radnor, PA, USA). The solution is seeded with lycopodium particles (Sigma-Aldrich) with a concentration of about 0.7 g.l^{-1}.

Planar velocity measurements are obtained using particle image velocimetry (PIV) (LaVision GMBH, Goettingen, Germany). The laser sheet emitted by a double Nd:YAG pulsed laser is reflected by the lycopodium particles. Images of the position of the particles are recorded by a
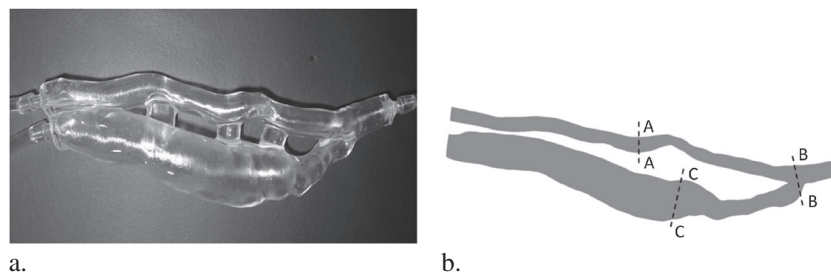

a.   b.

Figure 4. (a) Transparent phantom of the patient-specific arteriovenous fistula geometry. (b) Locations of the cutting lines along which the numerical and experimental velocity profiles are evaluated.
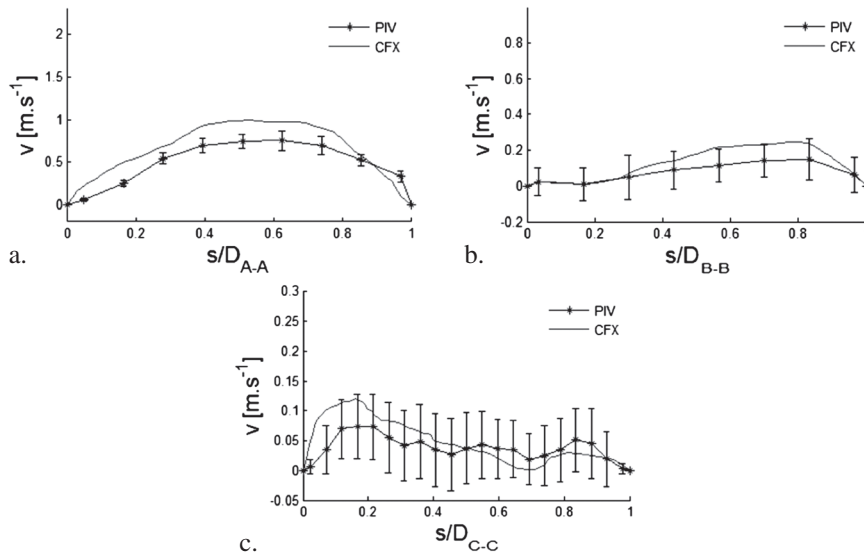
Figure 5. Comparison of the experimental (particle image velocimetry) and numerical (CFX) velocity profiles along the cutting lines defined in Figure 4(b). The error bars on the experimental data correspond to the SD of the measured velocities.

1660×1200 charge-coupled device camera (Image Pro X 2M, LaVision GMBH, Goettingen, Germany) at 28 frames.s^{-1}. The PIV data have been processed using a three-pass iteration technique with a constant-size 32×32 window and a 50% overlap. A median filter has been used to detect spurious velocity vectors; at each point, the velocity vector is compared to the median vector calculated with the eight neighboring ones. The point vector is deleted and replaced by the spatial mean if it is outside the deviation of the neighbors.

We have compared the velocity profiles obtained numerically and experimentally under the same flow conditions along specific cutting lines within the field of view. We have focused on three regions of interest: the stenosed radial artery, the anastomosis between the radial artery and the cephalic vein, and the enlarged cephalic vein (Figure 4(b)). For the PIV data, a zero velocity is imposed at the location of the vessel wall during post-treatment. Figure 5 shows the profiles of the velocity magnitude v as a function of the curvilinear abscissa s along the cutting line. The abscissa is non-dimensionalized by the vessel equivalent diameter in the cross-sectional plane ($D_{A-A} = 7.4$ mm, $D_{B-B} = 8.57$ mm, $D_{C-C} = 20.64$ mm). The superposition of the two velocity curves proves that the numerical simulation captures the flow behavior despite the complexity of the vessel geometry. The numerical predictions follow the same profiles as the experimental ones. The predicted values are all within the experimental uncertainty. The good fit between the numerical and experimental velocity profiles validates the numerical method used to simulate the flow within the AVF.

3. PATIENT-SPECIFIC FSI MODEL

3.1. Hemodynamics

The mean velocity entering the radial artery does not vary significantly over the cardiac cycle, which is typical of peripheral arterial flows; it ranges from 0.42 m.s^{-1} at peak diastole to 0.62 m.s^{-1} at peak systole. As a consequence, only moderate differences in the mean velocity are found over time across different segments of the AVF. In order to visualize the flow patterns, 31 velocity streamlines are shown at peak systole in Figure 6 and at late diastole in Figure 7. The stenosis causes a local increase in the flow velocity, as well as a region of recirculation downstream of it. The flow impacts on the bifurcation between the radial artery and cephalic vein, called the anastomosis, generating a stagnation point (red box in Figure 6).

The particularity of most mature AVFs is to present an enlarged vein; it is associated with the largest zone of flow recirculation. If we compare Figures 6 and 7, we observe a change in streamline
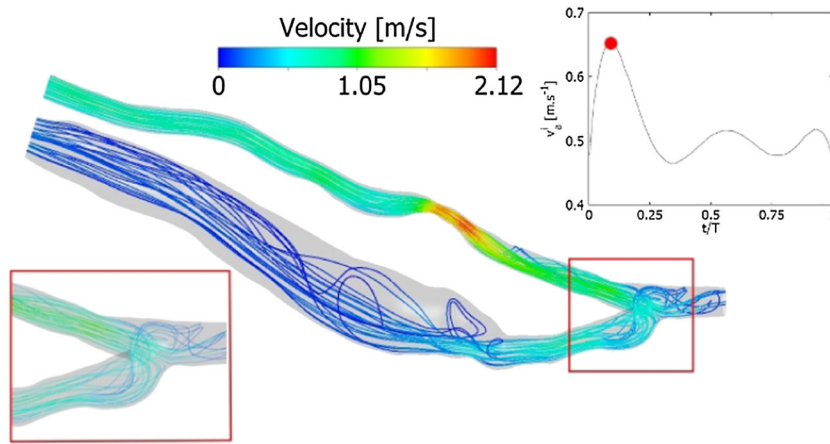
Figure 6. Velocity streamlines at peak systole. The time of measurement is indicated by the red dot on the inlet velocity profile. On the bottom left, a zoom on the region of the anastomosis shows that the flow impacts on the bifurcation generating a stagnation point.
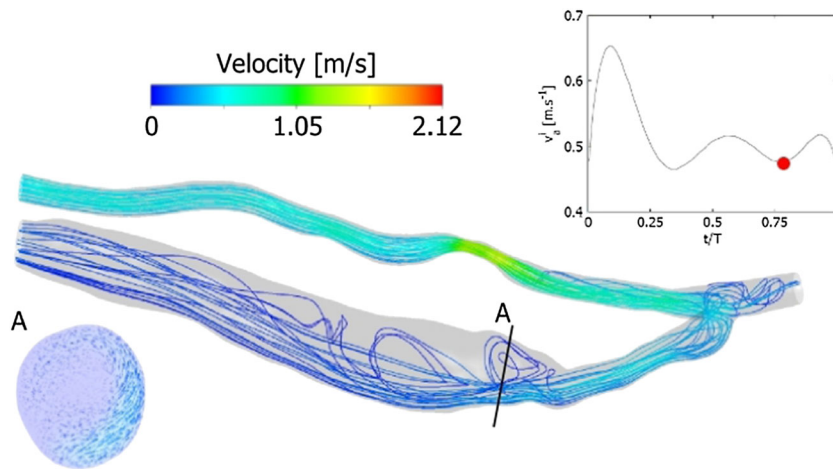

Figure 7. Velocity streamlines at late diastole. The red dot on the inlet velocity profile indicates the corresponding time of measurement. The bottom left insert shows the flow recirculation inside the vein (section plane A); the velocity arrows have been projected within the two-dimensional plane.

distribution in the cephalic vein with a stronger recirculation motion and helical flow at late diastole (shown in cross-section A, Figure 7).

We have analyzed the evolution of the static pressure along the vasculature. We observe a global static pressure drop between the arterial inlet and the venous outlet of 16.6 mmHg. About 70% of the pressure drop is caused by the stenosis. The vein enlargement does not lead to a significant additional pressure drop.

3.2. Wall shear stresses analysis

Wall shear stresses
The WSS map is shown in Figure 8. The WSS values fall within the healthy physiological range in the proximal radial artery, upstream of the stenosis. Still, the vessel tortuosity leads locally to WSS up to 10 Pa. The highest WSS is found at the level of the stenosis, where it approaches 60 Pa. The anastomosis is the other region subjected to high WSS ($\approx$ 18 Pa) especially on its venous side; it is a consequence of the incoming flow impacting onto the bifurcation. Lee and

Roy-Chaudhury [37] have suggested that the large WSS lead to an increase in the oxidative stress resulting in inflammation and peri-anastomotic neo-intimal formation.
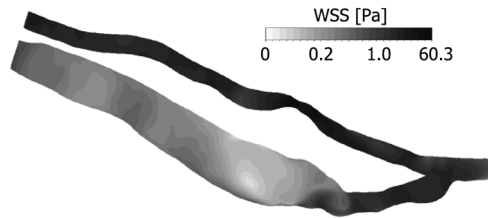

Figure 8. Wall shear stresses map (WSS) at peak systole. The highest WSS are found at the stenosis. A logarithmic gray-scale has been used to highlight the low WSS values calculated in the enlarged region of the vein.

On the venous side, the patient presents a venous enlargement over most of the cephalic vein. This entire region is subjected to WSS generally below 0.15 Pa and OSI values larger than 0.4 Pa (Figure 9). The combination of extremely low WSS and high OSI values has been associated with intima hyperplasia [35].

Wall shear stress time derivatives. In the case of AVF, time derivatives have been shown to have a larger influence than spatial gradients [38, 39]. We will therefore concentrate on the WSS time derivative $WSSG_t$. WSS_t are about nil across the AVF (data not shown) apart from two locations (Figure 10). The region that experiences particularly high $WSSG_t$ with large temporal variations is the anastomosis (point B in Figure 1). The second highest value is found in the enlarged venous region (point C in Figure 1), but the maximum amplitude is only 10 Pa.s^{-1}, and the variations appear mainly in the diastolic phase of the cardiac cycle. Previous studies have associated WSS time derivatives with endothelial cell proliferation and neo-intimal formation [39]. A thicker neo-intimal layer may modify the flow split in the long run by altering the vessel resistances. It could thus have large clinical consequences: on the one hand, too low arterial flow can cause necrosis of hand tissues; on the other hand, too low venous flow prevents the hemodialysis from taking place.

3.3. Internal wall stresses analysis

The map of vascular wall displacement is represented at peak systole in Figure 11. The maximum displacement in the artery is 0.62 mm, which corresponds to a maximum strain of 14%. On average, the strain in the artery is of the order of 10%. It is about eight times smaller in the vein, which is a consequence of the larger stiffness of the venous wall. In the vein, the maximum displacement is only about 0.05 mm, (maximum strain of 3%). We have analyzed the corresponding values of the maximum component of the principal stresses $\overline{\sigma}_{max}$ at the vascular wall at peak systole. Because the distribution resembles the map of wall distribution shown in Figure 11, we only indicate values in the various zones. The maximum principal stresses fall in the range 5.5–7.0 kPa inside the artery, with a space-averaged value of 5.7 kPa. Within the cephalic vein, they are equal to 8.0–13.5 kPa with a space-averaged value of 11.5 kPa.

We hypothesize, based on the results of previous studies [40–42], that healthy large vessels remodel their internal structure to achieve a quasi-uniform internal stress of constant value. To determine this baseline stress value, we have considered the part of the radial artery located 8 to 16 diameters from S_a^i, i.e. where the flow is fully-developed and unperturbed by the stenosis. This region is also the least influenced by the existence of the anastomosis. Figure 12 shows the internal wall stresses normalized by the baseline stress. Results show that the stresses inside the venous wall are, on average, larger than their baseline value by a factor of 2 and that they can be up to 2.4 times larger.

Non-physiological internal wall stresses can generate wall remodeling through their impact on smooth muscle cells; the cells are responsive to the level of stresses and modulate their migration rate, proliferation, and synthesis of collagen [40, 43, 44]. One limitation that we face to analyze the
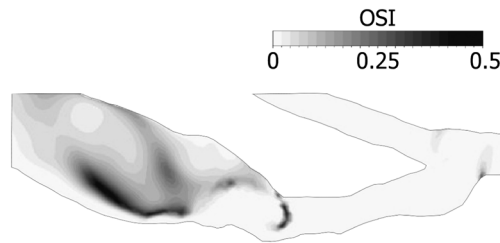
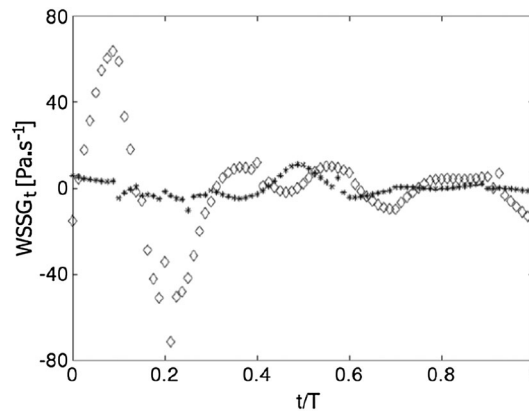Figure 9. Oscillatory shear index spatial distribution in the cephalic vein.

Figure 10. $WSSG_t$ time variation at point B in the anastomosis ($\diamond$) and point C in the vein enlargement ($*$). Points B and C are defined in Figure 1.

present results is that most of the research on wall remodeling has been conducted in arteries, which are muscular vessels. Less is known on the remodeling of veins. Still, the last four decades of clinical practice of AVF prove the high capability of remodeling of veins under increased hemodynamic stresses, because veins are able to get arterialized over a period of 3–6 months [4, 24]. We presently find non-nominal values of internal wall stress in the cephalic vein, which would indicate that the vein continues its remodeling. This perpetuation of the phenomenon could result in excessive wall remodeling downstream of the anastomosis and explain the enlargement of the vein.

4. RELAXATION OF VARIOUS HYPOTHESES IN THE SIMULATION

In the previous section, we have shown that although feasible, a coupled fluid-structure simulation is highly challenging and results in large computational times. The calculation takes 70 CPU hours to run on two cores. The objective is to eventually translate the simulation tool to clinicians, but a routine use will not be possible in practice if the computational time is not reduced. In this section, we investigate whether it is possible to reduce the computational time by relaxing some
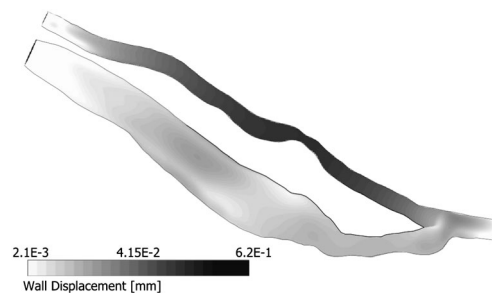

Figure 11. Spatial distribution of the vascular wall displacement. The map is shown in a logarithmic scale.

of the hypotheses while maintaining the clinical relevance of the simulation. We will compare the more comprehensive patient-specific model (Section 3) with simulations assuming first blood to be Newtonian, and secondly, the vessels to have uniform properties (same thickness and mechanical properties all along the vasculature). We will then evaluate the accuracy of uncoupled fluid or structural simulations.

4.1. Comparison between Newtonian and non-Newtonian blood modeling

Blood is a non-Newtonian fluid, but in some cases it is known that its non-Newtonian behavior may be neglected. From a numerical point of view, the main problem of implementing a non-linear Casson model is the numerical instability that it induces. But once the non-Newtonian simulation is rendered stable, its computational time is comparable to that of the Newtonian case.

To investigate the relevance of modeling the non-Newtonian blood behavior, let us first represent the equivalent dynamic viscosity values along the AVF wall calculated using equation (2). The local dynamic viscosity is function of the local shear rate. Inside the radial artery, where the maximum shear rate is equal to 300 s^{-1}, the dynamic viscosity is equal to 3.2×10^{-3} Pa.s^{-1} (Figure 13). It corresponds to the asymptotic viscosity imposed in the model for large shear-rates, when the fluid follows a Newtonian behavior. Within the enlarged vein, the non-Newtonian effects are, however, significant; as shear rates are lower than 100 s^{-1}, the equivalent dynamic viscosity becomes up to six times larger than within the artery.

We have run a new simulation, in which blood is set to be Newtonian with a dynamic viscosity $\mu = 3.2 \times 10^{-3}$ Pa.s (same value as that of the Casson model at large shear rates). All the other parameters of the simulation are otherwise identical to the reference case (Section 3). We have quantified the difference in WSS magnitude between both models. Inside the proximal artery, the difference is basically non-existant. The largest difference in spatial-averaged WSS is found in the enlarged vein; at this location, we observe a mean difference of 13%, with local peaks at 20%. At the anastomosis, the difference is about 15%, with a spatial average of 10%. This is coherent with the findings of Kabinejadian and Ghista [45].
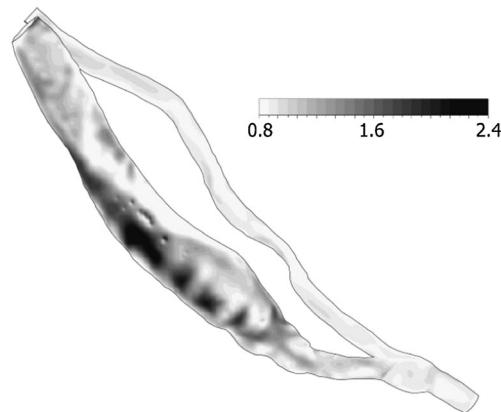

Figure 12. Spatial distribution of the internal wall stresses $\overline{\sigma}_{max}$ normalized by the baseline stress.
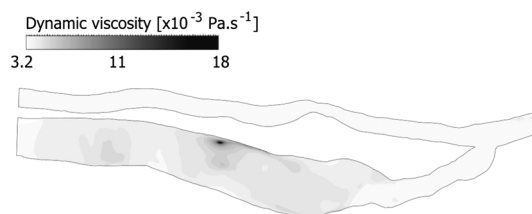

Figure 13. Dynamic viscosity values obtained at the arteriovenous fistula wall with the Casson's model.

The choice of the non-Newtonian model is therefore justified by the low shear rate conditions that prevail inside the cephalic vein and lead to significant non-Newtonian effects. In this region, the WSS would be overestimated by a Newtonian model. As previously shown by Merril and Schmid-Schonbein [28, 46], blood behaves in a Newtonian fashion under shear rates larger than $150 - 300$ s^{-1}, which is typically the case in arteries with a diameter larger than 0.5 mm. A shear rate value of 100 s^{-1} has been identified as the threshold below which non-Newtonian effects need to be modeled, but they begin to be significant for shear rates $\dot{\gamma} \leqslant 150$ s^{-1}.

4.2. Comparison between the reference case and a homogeneous wall model

Differentiating arterial and venous wall properties substantially increases the time of preparation of the simulation and therefore the probability to introduce numerical errors. It indeed requires to segment the vascular geometry into different sub-parts, to which different properties are assigned. In order to ensure the numerical stability, one also needs to guarantee the correspondence of the boundary nodes between the segmented parts and their connection during the simulation.

In this sub-section, we aim at estimating the error on the hemodynamics and wall mechanics, if one models the vessel wall with uniform properties. A new simulation is run imposing the entire vascular wall to have the arterial geometrical and mechanical properties described in Section 2.3. Blood is still supposed to follow the Casson model. The same fluid and solid mechanics boundary conditions are imposed as for the reference case (Section 3).

Comparing the overall hemodynamic conditions predicted by both simulations, we only observe small differences. The error on the flow rate entering the cephalic vein at the anastomosis is inferior to 1%, and no difference is calculated on the venous WSS. The maximum error is found on the hemodynamic conditions predicted at the stenosis; the uniform wall simulation overestimates the WSS by 14%, and underestimates the stenosis pressure drop by 7.5% (Table III). The latter is shifted in time and occurs at $t/T = 0.25$ instead of $t/T = 0.15$ in the reference case. This is a consequence of the smaller venous compliance.

More significant is the effect on the internal maximum principal stresses. When one models the vein with compliance and thickness identical to the arterial one, one obtains non-dimensional internal stresses close to 1; they appear to be in the physiological range. We have independently studied the influence of wall thickness and have seen that its contribution is negligible on the hemodynamics and weights for less than 2% on the maximal wall internal stresses values (data not shown). We conclude that it is necessary to impose wall properties that are as realistic as possible in order to properly estimate the risk of perpetuation of wall remodeling in the vein clinically. This is important, all the more so as it does not increase the computational time.

The main limitation of this conclusion is the difficulty in estimating the actual venous wall properties; the tissue is that of a vein subjected to arterial hemodynamic conditions. It is impossible to infer its properties from measurements on other venous tissues. Furthermore, the vein appears to be in constant remodeling, suggesting that its properties evolve over time.

4.3. Comparison between FSI and uncoupled fluid or structural simulations

To quantify the influence of wall compliance on the hemodynamics, we have conducted a CFD simulation using the fluid solver ANSYS CFX (ANSYS, Inc.). The rigid wall CFD simulation has been performed using the same settings for ANSYS-CFX as in the FSI simulation but deactivating

Table III. Comparison of the results provided in the reference case and in the case of homogeneous wall properties at peak systole.

Parameter	Reference Case	Homogeneous Wall
Velocity at stenosis	2.12 m·s^{-1}	2.11 m·s^{-1}
WSS at stenosis	60.3 Pa	69.2 Pa
$\overline{\sigma}_{max}$ normalized by baseline stress	≈ 2	≈ 0.9

Table IV. Comparison of the results provided in the reference case (FSI simulation) and in the rigid-wall case (CFD simulation) at peak systole.

Parameter	FSI	CFD
Velocity at stenosis	2.12 m·s^{-1}	2.52 m·s^{-1}
WSS **at stenosis**	60.3 Pa	69.3 Pa
Flow rate percentage in cephalic vein	$\approx 70\%$	$\approx 68\%$

the multifield coupling. In particular, we have imposed the same boundary conditions described in Section 2.5 and similarly assumed blood to follow the Casson model.

Comparing the two simulations, we notice that the local velocity and *WSS* values are globally overestimated by the CFD study. The largest differences found at peak systole are indicated in Table IV. The rigid-wall simulation overestimates the peak velocity at the stenosis by $\approx 20\%$ and the peak *WSS* values by $\approx 15\%$. The differences are, however, of a much smaller extent ($\approx 2\%$) in the zones of low velocity and *WSS*. The flow distribution across the two exits is well predicted (error $\leqslant 2\%$).

Although the quantitative data fail in accuracy, the CFD simulation provides a coherent qualitative picture of the hemodynamic conditions that prevail in the vasculature. It gives sound predictions for the zones dominated by low hemodynamic conditions. These zones have a high clinical relevance, because they are prone to complications, such as neo-intimal formation. Another advantage is the computational time, the rigid-wall simulation running 12 times faster than the fully-coupled FSI.

We have independently run a structural static simulation (ANSYS-Mechanical; ANSYS, Inc.). Instead of running the simulation with a two-way coupling as for the FSI simulation, we have presently used a weak one-way coupling. This method enables to impose the distribution of pressure at the AVF internal vessel walls calculated by the CFD simulation at a given instant of time. We have run the structural simulation with the peak systolic pressure field as lateral boundary condition. All the other boundary conditions are kept unchanged. The analysis of the wall displacement and internal constraints show that the difference with the reference case at peak systole is below 1% all along the vasculature. The structural simulation therefore predicts the results very accurately. It, however, cannot provide directly the time-evolution of the wall displacement and stresses. Such as for the CFD simulation, the computational time is drastically reduced; the structural simulation runs in only one hour.

5. DISCUSSION AND CONCLUSION

We have modeled the FSI in a patient-specific AVF geometry, modeling the vessel wall with non-uniform hyperelastic properties and the non-Newtonian behavior of blood. We have differentiated the venous and arterial mechanical properties in order to obtain realistic results for the internal stresses in the vascular wall.

Our results confirm that AVFs are subjected to complex hemodynamics. The enlarged portion of the cephalic vein is subjected to *WSS* smaller than a tenth of the physiological values and *OSI* larger than 0.4. It also experiences non-zero time derivatives of *WSS*. The anastomosis is subjected to a stagnation point flow along with high time derivatives of *WSS*. These regions are therefore the more likely to suffer from intima hyperplasia.

The simulation has shown that the cephalic vein is conjointly subjected to internal wall stresses that are about the double to their baseline level. This condition is likely to promote continuous remodeling of the wall internal structure and therefore represents a risk of AVF failure.

Such an FSI patient-specific simulation is challenging in many aspects. The first issue is to reconstruct the vascular geometry from medical images. Even with the greatest care, it is not easy to ensure that the vessel geometry obtained through the segmentation and reconstruction procedures is identical to the one observed clinically. It may sometimes be difficult to isolate the blood lumen from surrounding tissues on the scan images and therefore to automatize the process. Then the FSI simulation itself is complicated owing to the large region of interest, the non-linear effects of the

fluid and solid constitutive laws and the instabilities of the FSI coupling. We have, however, proven that it is feasible to solve the multi-physics numerical simulation using the commercial environment provided by ANSYS, Inc.

Setting relevant mechanical properties for the different vessel portions has proven to suffer from the lack of available data in the literature. It is known that the vein is subjected to a significant increase in stiffness as a consequence of the fragmentation of the elastin content and increase in collagen content, as the vein enlarges [24, 47]. But few quantitative data exist as reported in the introduction. Similarly, it has not been possible to take into account the presence of external tissues to the AVF; no study has yet characterized the mechanical properties of the tissues below the elbow region.

In order to evaluate the importance of taking all the modeling components into account, we have compared the results with simplified versions of the simulation and come to the following conclusions:

– A non-Newtonian blood model is needed to predict the hemodynamics in the venous part of the AVF, owing to the low values of shear rates. The Casson model is, however, not useful on the arterial side.
– The use of homogeneous wall properties simplifies the preparation of the model, but does not provide a significant gain in computational time. It, however, significantly underestimates the internal wall stresses. When simulating the FSI in an AVF, one needs to take into account the very different wall properties of the venous and arterial parts of the vasculature. Such an issue will also come into play for other vascular diseases that profoundly alter the vessel mechanical properties over an extended region.
– Although the CFD simulation generally overestimates velocities and WSS, it still gives an informative map of the regions affected by WSS values, which can lead to neo-intimal formation.
– A one-way coupling structural simulation provides the precise distribution of internal wall stresses, but only at one instant of time. It does not provide the time evolution of the stress distribution.
– Running an uncoupled fluid and structural simulation has the advantage to run significantly faster than the FSI simulation (15 h instead of 70 h).

The advantages and disadvantages of each simplified model are summarized in Table V.

The present study proves that a full FSI study is not always needed. Because the vessel wall deformability has a limited influence on the blood flow dynamics, fluid-only simulations appear to be efficient at providing a qualitative relevant hemodynamic map. The error made on the WSS values by neglecting the wall deformation is down to a few percent in most cases. Conversely, a solid-only simulation may be sufficient to estimate the maximum internal wall stresses. Still, FSI simulations have the advantage of providing the time-evolution of both the fluid and structural

Table V. Advantages and disadvantages related to each simplified model.

Model	Advantages	Disadvantages
Non-Newtonian blood behavior	Captures flow characteristics of the venous part	Not useful on the arterial side
Homogeneous wall properties	–	Incorrect estimation of WSS and wall internal stresses
CFD	Qualitative picture of overall flow characteristics + gain in computational time	No information on internal wall stresses
Structure only	Precise internal wall stress distribution	No information on time-evolution
Uncoupled fluid and structure	Faster to run than fully-coupled FSI	Iterative process to obtain the same amount of data

stresses. Their resolution is also required in the case of compliant vessel walls (e.g., venous circulation). In the future, it would be interesting to design new techniques to characterize the tissues *in vivo* non-invasively. This is a necessary step for clinicians to one day fully rely on the results of numerical simulations in the making of therapeutic choices.

REFERENCES

1. Allon M, Robbin ML. Increasing arteriovenous fistulas in hemodialysis patients: problems and solutions. *Kidney International* 2002; **62**:1109–1124.
2. Kian K, Vassalotti JA. The new arteriovenous fistula: the need for earlier evaluation and intervention. *Seminars in Dialysis* 2005; **18**:3–7.
3. Sivanesan S, How TV, Black RA, Bakran A. Flow patterns in the radiocephalic arteriovenous fistula: an in vitro study. *Journal of Biomechanics* 1999; **32**(9):915–925.
4. Dixon BS. Why don't fistulas mature? *Kidney International* 2006; **70**:1413–1422.
5. Ponikvar R. Surgical salvage of thrombosed native arteriovenous fistulas for hemodialysis by interventional nephrologists. *Ther Apher Dial* 2009; **13**:340–344.
6. vanTricht I, DeWachter D, Tordoir J, Verdonk P. Hemodynamics and complications encountered with arteriovenous fistulas and grafts as vascular access for hemodialysis: a review. *Annals of Biomedical Engineering* 2005; **33**:1142–1157.
7. Wan M, Gong X, Qian M. In vivo hemodynamic evaluation based on transverse doppler measurements of blood velocities and vessel diameter. *IEEE Transactions Biomedical Engineering* 1999; **46**:1074–1080.
8. Ene-Iordache B, Mosconi L, Remuzzi G, Remuzzi A. Computational fluid dynamics of a vascular access case for hemodialysis. *Journal of Biomechanical Engineering* 2001; **123**:284–292.
9. Kharboutly Z, Fenech M, Treutenaere JM, Claude I, Legallais C. Investigations into the relationship between hemodynamics and vascular alterations in an established arteriovenous fistula. *Medical Engineering & Physics* 2007; **29**:999–1007.
10. Niemann AK, Thrysoe S, Nygaard JV, Hasenkam JM, Petersen SE. Computational fluid dynamics simulation of a-v fistulas: from MRI and ultrasound scans to numeric evaluation of hemodynamics. *Journal of Vascular Access* 2011; **13**:36–44.
11. Chen J, Wang S, Ding G, Yang X, Li H. The effect of aneurismal-wall mechanical properties on patient-specific hemodynamic simulations- two clinical case reports. *Acta Mechanica Sinica* 2009; **25**:677–688.
12. Gerbeau J-F, Vidrascu M, Frey P. Fluid structure interaction in blood flow on geometries based on medical images. *Computers & Structures* 2005; **83**:155–165.
13. Kim YH, Kim JE, Ito Y, Shih AM, Brott B, Anayiotos A. Hemodynamic analysis of a compliant femoral artery bifurcation model using a fluid structure interaction framework. *Annals of Biomedical Engineering* 2008; **36**:1753–1763.
14. Li Z, Kleinstreuer C. Fluid-structure interaction effects on sac-blood pressure and wall stress in a stented aneurysm. *Journal of Biomechanical Engineering* 2005; **127**:662–671.
15. Tang D, Yang C, Kobayashi S, Zheng J, Woodard PK, Teng Z, Billiar K, Bach R, Ku DN. 3D MRI-based anisotropic FSI models with cyclic bending for human coronary atherosclerotic plaque mechanical analysis. *Journal of Biomechanical Engineering* 2009; **131**:061010.
16. Tezduyar TE, Sathe S, Schwaab M, Conklin BS. Arterial fluid mechanics modeling with the stabilized space-time fluide-structure interaction technique. *International Journal for Numerical Methods in Fluids* 2008; **57**:601–629.
17. Torii R, Wood NB, Hadjiloizou N, Dowsey AW, Wright AR, Hughes AD, Davies J, Francis DP, Mayet J, Yang GZ, Thom SM, Xu XY. Fluid–structure interaction analysis of a patient-specific right coronary artery with physiological velocity and pressure waveforms. *International Journal for Numerical Methods in Biomedical Engineering* 2009; **25**:565–580.
18. Molony DS, Callanan A, Kavanagh EG, Walsh MT, McGloughlin TM. Fluid-structure interaction of a patient-specific abdominal aortic aneurysm treated with an endovascular stent-graft. *BioMedical Engineering OnLine* 2009; **6**:8–24.
19. Tang D, Yang C, Mondal S, Liu F, Canton G, Hatsukami TS, Yuan C. A negative correlation between human carotid atherosclerotic plaque progression and plaque wall stress: in vivo MRI-based 2D/3D FSI models. *Journal of Biomechanics* 2008; **41**(4):727–736.
20. Taylor CA, Figueroa CA. Patient-specific modeling of cardiovascular mechanics. *Annual Review of Biomedical Engineering* 2009; **11**:109–134.

21. Torii R, Oshima M, Kobayashi T, Takagi K, Tezduyar TE. Computer modeling of cardiovascular fluid-structure interactions with the deforming-spatial-domain/stabilized space-time formulation. *Computer Methods in Applied Mechanics and Engineering* 2006; **195**(13–16):1885–1895.

22. Xiong G, Figueroa CA, Xiao N, Taylor CA. Simulation of blood flow in deformable vessels using subject-specific geometry and spatially varying wall properties. *International Journal for Numerical Methods in Biomedical Engineering* 2011; **27**:1000–1016.

23. Kharboutly Z, Treutenaere JM, Claude I, Legallais C. Arterio-venous fistula: two cases realistic numerical blood flow simulations. *Proceedings of the 29th Annual International Conference of the IEEE EMBS, Lyon, France,* August 23–26 2007; 2980–2983.

24. Corpataux JM, Haesler E, Silacci P, Ris HB, Hayoz D. Low-pressure environment and remodelling of the forearm vein in brescia-cimino haemodialysis access. *Nephrology Dialysis Transplantation* 2002; **17**:1057–1062.

25. Gutierrez MA, Pilon PE, Lage SG, Kopel L, Carvalho RT, Furuie SS. Automatic measurement of carotid diameter and wall thickness in ultrasound images. *Computing in Cardiology* 2002; **29**:359–362.

26. Rohlf K, Tenti G. The role of the Womersley number in pulsatile blood flow: a theoretical study of the Casson model. *Journal of Biomechanics* 2001; **34**:141–148.

27. Boyd J, Buick JM, Green S. Analysis of the Casson and Carreau-Yasuda non-Newtonian blood models in steady and oscillatory flows using the lattice Boltzmann method. *Physics of Fluids* 2007; **19**:093103.

28. Merril EW, Pelletier GA. Viscosity of human blood: transition from Newtonian to non-Newtonian. *Journal of Applied Physiology* 1967; **23**:178–182.

29. Yeoh OH. Some forms of the strain energy function for rubber. *Rubber Chemistry and Technology* 1993; **66**:754–771.

30. McGilvray KC, Sarkar R, Nguyen K, Puttlitz CM. A biomechanical analysis of venous tissue in its normal and post-phlebitic conditions. *Journal of Biomechanics* 2010; **43**:2941–2947.

31. Prendergast PJ, Lally C, Daly S, Reid AJ, Lee TC, Quinn D, Dolan F. Analysis of prolapse in cardiovascular stents: a constitutive equation for vascular tissue and finite-element modelling. *Journal of Biomechanical Engineering* 2003; **125**:692–699.

32. Womersley JR. Method for the calculation of velocity, rate of flow and viscous drag in arteries when the pressure gradient is known. *Journal of Physiology* 1955; **28**:553–563.

33. ANSYS Academic Research, Release 13.0, Help System, ANSYS Inc., 2010. [28 February 2011].

34. Rhie CM, Chow WL. Numerical study of the turbulent flow past an airfoil with trailing edge separation. *AIAA Journal* 1983; **21**:1525–1532.

35. Jackson M, Wood NB, Zhao S, Augst A, Wolfe JH, Gedroyc WMW, Hughes AD, Thom SAMcG, Xu XY. Low wall shear stress predicts subsequent development of wall hypertrophy in lower limb bypass grafts. *Artery Research* 2009; **3**:32–38.

36. Chiu JJ, Chien S. Effects of disturbed flow on vascular endothelium: pathophysiological basis and clinical perspectives. *Physiological Reviews* 2011; **91**:327–387.

37. Lee T, Roy-Chaudhury P. Advances and new frontiers in the pathophysiology of venous neointimal hyperplasia and dialysis access stenosis. *Advances in Chronic Kidney Disease* 2009; **16**:329–338.

38. Ojha M. Wall shear stress temporal gradient and anastomotic intimal hyperplasia. *Circulation Research* 1994; **74**:1227–1231.

39. Markl M, Wegent F, Zech T, Bauer S, Strecker C, Schumacher M, Weiller C, Hennig J, Harloff A. In vivo wall shear stress distribution in the carotid artery: effect of bifurcation geometry, internal carotid artery stenosis, and recanalization therapy. *Circulation: Cardiovascular Imaging* 2010; **3**:647–655.

40. Rachev A. Theoretical study of the effect of stress-dependent remodeling on arterial geometry under hypertensive conditions. *Journal of Biomechanic* 1997; **30**(8):819–827.

41. Glagov S, Zarins CK, Masawa N, Xu CP, Bassiouny H, Giddens DP. Mechanical functional role of non-atherosclerotic intimal thickening. *Frontiers of Medical & Biological Engineering* 1993; **5**:37–43.

42. Fridez P, Zulliger M, Bobard F, Montorzi G, Miyazaki H, Hayashi K, Stergiopulos N. Geometrical, functional, and histomorphometric adaptation of rat carotid artery in induced hypertension. *Journal of Biomechanics* 2003; **36**:671–680.

43. Rachev A, Stergiopulos N, Meister J-J. Theoretical study of dynamics of arterial wall remodeling in response to changes in blood pressure. *Journal of Biomechanics* 1996; **29**(5):635–642.

44. Martinez-Lemus LA, Hill MA, Meininger GA. The plastic nature of the vascular wall: a continuum of remodeling events contributing to control of arteriolar diameter and structure. *Physiology* 2009; **24**:45–57.

45. Kabinejadian F, Ghista DN. Compliant model of a coupled sequential coronary arterial bypass graft: effects of vessel wall elasticity and non-newtonian rheology on blood flow regime and hemodynamic parameters distribution. *Medical Engineering & Physics* 2011; **34**:860–872.

46. Schmid-Schonbein H, Gaehtgens P, Hirsch H. On the shear rate dependence of red cell aggregation in vitro. *Journal of Clinical Investigation* 1968; **47**:1447–1454.

47. Kritharis EP, Kakisis JD, Giagini AT, Manos T, Stergiopulos N, Tsangaris S, Sokolis DP. Biomechanical, morphological and zero-stress state characterization of jugular vein remodeling in arteriovenous fistulas for hemodialysis. *Biorheology* 2010; **47**(5-6):297–319.